



Aluminium doped ZnO nanostructures for efficient photodegradation of indigo carmine and azo carmine G in solar irradiation

Abhishek R. Bhapkar¹ · Mithra Geetha² · Dipika Jaspal¹ · Khalil Gheisari³ · Meena Laad¹ · John-John Cabibihan⁴ · Kishor Kumar Sadasivuni² · Shekhar Bhamé¹

Received: 11 December 2022 / Accepted: 4 March 2023 / Published online: 20 March 2023
© The Author(s) 2023

Abstract

Aluminium doped zinc oxide (AZO) nanomaterials ($\text{Al}_x\text{Zn}_{1-x}\text{O}$) with x fraction varying as 0.02 and 0.04 were synthesized using the auto-combustion method using glycine as a fuel. The synthesized catalysts were characterized with X-ray diffraction (XRD), UV–Visible Spectroscopy (UV–Vis), Raman spectroscopy, Photoluminescence (PL) spectroscopy, and High Resolution Transmission Electron Microscopy (HR-TEM). XRD results showed that synthesized materials possessed good crystallinity, while UV–VIS was employed to find the band gaps of synthesized materials. Raman was used to determine the vibrational modes in the synthesized nanoparticles, while TEM analysis was performed to study the morphology of the samples. Industrial effluents such as indigo carmine and azo carmine G were used to test the photodegradation ability of synthesised catalysts. Parameters such as the effect of catalyst loading, dye concentration and pH were studied. The reduction in crystallite size, band gap and increased lattice strain for the 4% AZO was the primary reason for the degradation in visible irradiation, degrading 97 and 99% equimolar concentrations of indigo carmine and azo carmine G in 140 min. The Al doped ZnO was found to be effective in faster degradation of dyes as compared to pure ZnO in presence of natural sunlight.

Keywords Photocatalysis · Zinc oxide · Aluminium doped zinc oxide · Indigo carmine · Azocarminé G · Photodegradation

Introduction

Industrialization has resulted in a significant increase in the presence of potentially carcinogenic intermediates in dyes, pesticides, phenols, solvents, and other organic pollutants in natural resources (Jiang et al. 2005). The presence of organic dyes in industrial wastewaters from the textile, paper, and apparel industries, in particular, results in significant

environmental contamination (Rafiq et al. 2021). Dyes like Indigo Carmine, Azo Carmine G, Methylene Blue, Rhodamine B, Eriochrome Black-T (EBT), Rose Bengal, and Thymol blue are used in the textile industry every year (Wahba et al. 2020; El-Samak et al. 2022; Sharma et al. 2015; Huang et al. 2017; Najjar et al. 2021; Kazeminezhad and Sadollahkhani 2016; Balouch et al. 2022), and most of it ends up in wastewater (Kumar 2017). These dye-polluted effluents are harmful to living organisms since they contain highly toxic, non-biodegradable pigments (Saidani et al. 2017; Umar et al. 2022). Even at very low concentrations (1 ppm), dyes are clearly visible in water and cause water pollution (Daneshvar et al. 2004). According to the World Bank, dyeing industries and textile finishing contribute approximately 17–20% of water pollution. Kant reported that, of the identified major wastewater contaminants, textile dyeing released 72 chemicals, where more than 30 of these were found to be hazardous in nature (Kant 2012). Hence removal of dye from wastewater is given preference in recent times.

To address this issue, several approaches have been taken, including adsorption, coagulation, membrane separation, and photocatalytic degradation, etc. (Thamaraiselvan and

✉ Kishor Kumar Sadasivuni
kishor_kumars@yahoo.com

✉ Shekhar Bhamé
shekhar.bhame@sitpune.edu.in

¹ Symbiosis Institute of Technology, Symbiosis International (Deemed University), Pune, India

² Center for Advanced Materials, Qatar University, P. O. Box 2713, Doha, Qatar

³ Department of Materials Science and Engineering, Faculty of Engineering, Shahid Chamran University of Ahvaz, Ahvaz, Iran

⁴ Department of Mechanical and Industrial Engineering, Qatar University, P.O. Box 2713, 2713 Doha, Qatar

Noel 2015; Kasperchik et al. 2012; Shah et al. 2020). The photocatalytic transformation of organic pollutants into non-toxic molecules is one of the most widely researched topics. In 1972, Fujishima and Honda explored the phenomenon of photocatalytic water splitting using UV light on TiO₂ electrodes (Fujishima and Honda 1972). This discovery ushered in a new era of heterogeneous photocatalysis. TiO₂ has been the most worked upon photocatalyst from its early development in the 1970s due to its comparatively availability, low cost, and high efficiency (Hernández-Alonso et al. 2009). Despite being the good photocatalyst, several factors such as lower cost, higher surface reactivity, similar band gap, and better degradation rate at the beginning have made ZnO a viable alternative to TiO₂ (Ganesh et al. 2018; Chandio et al. 2022). The faster recombination rate of the photo-generated electron–hole pair, on the other hand, reduces ZnO's photocatalytic activity and makes it unsuitable for practical applications.

Various synthesis methods such as hydrothermal, co-precipitation, sonochemical, sol–gel, polyol, combustion, electrochemical etc. have been employed in the past for the synthesis of ZnO nanoparticles (Gerbreder et al. 2020; Adam et al. 2018; Davis et al. 2019; Almezahia et al. 2022; Mika et al. 2019; Bhatti et al. 2022). The glycine nitrate synthesis is the technique in which oxidizer such as a metal nitrate and a fuel i.e. glycine, undergo self-sustained reaction. Glycine provides the energy required for combustion while also acting as a complexing agent (Jadhav et al. 2011). The advantage of glycine assisted synthesis is that the spontaneous evolution of a gaseous products during combustion dissipates heat from the process and limits increasing temperature, reducing the possibility of local sintering among particles while facilitating fine powder formation (Lim et al. 2019; Cheng et al. 2020).

Significant research has been conducted in order to improve the photocatalytic activity of ZnO by lowering the rate of photo-generated carrier recombination. Several techniques, such as modification of particle size (Retamoso et al. 2019), introduction of surface defects (Bai et al. 2013), doping with rare-earth lanthanides (Marin et al. 2019; Pascariu et al. 2019; Selvaraj et al. 2022), transition metals (Hossienzadeh et al. 2019; Liu et al. 2018), or composites with different semiconductors (Zouhier et al. 2020; Prabhuraj et al. 2021) etc. were used to improve the photodegradation efficiency of ZnO. Doping is a simple and effective method for increasing ZnO's photocatalytic activity because it involves a change in optical, electrical, and magnetic properties. Doping of semiconductor results in (i) band gap modification, (ii) enhanced photocatalytic efficiency that involves formation of charge traps for photo-generated carriers that suppresses the charge carrier recombination, and (iii) formation of intrinsic defects such as Zn interstitials and oxygen vacancies (Moiz et al. 2021; Pramanik et al. 2022). Various metals, including

Mn (Ma et al. 2016), Bi (Chandraboss et al. 2013), Co (Lu et al. 2011), Cu (Jiang et al. 2019), Cr (Chang et al. 2014a), Ce (Chang et al. 2014b), Ag (Hsu and Chang 2014), Al (Kuo et al. 2006), Ni (Zhao et al. 2011), etc. have been used to improve the photocatalytic activity of ZnO. Al is regarded as a suitable choice for dopant materials among the available alternatives (Luo et al. 2017). Due to its ease of availability and non-toxicity, Al doping has been carried out dominantly by researchers and is found to be effective in tuning the band gap ZnO (Prasad et al. 2018). Therefore, Al doped ZnO (AZO) is investigated for photocatalytic application in the present study. Among the various types, indigo carmine is a dye which is primarily used in textile industry to dye denims. It also finds applications in food, leather and pharmaceutical industries as colorant (Tabti et al. 2022). It is considered to have a very strong resistance to external conditions and retains the colour over longer periods of time. Because of its frequent use and toxic effects on aquatic ecosystems, indigo carmine is regarded as a contaminant that must be treated before wastewater is discharged (El-Kammah et al. 2022). Azo dyes are a major class of synthetic organic compounds that are widely used in textile, printing, pharmaceutical, and research laboratories. It can enter the human body through the skin and cause vomiting, lung tissue destruction, and rapid heart rate (Ai et al. 2011). Hence, azo carmine G was also chosen as a model pollutant in this study.

The current study seeks to synthesise ZnO nanomaterials using a low-cost glycine nitrate auto-combustion technique and to investigate the effect of Al doping on the optical, photocatalytic and structural properties of ZnO. The synthesized nanoparticles were characterized using XRD, UV–Vis, PL, Raman, HR-TEM and their photodegradation ability was tested with textile industrial dyes indigo carmine and azo carmine under sunlight irradiation. Both dyes are widely used in the textile industry, and they were chosen because they are understudied, allowing for a better understanding of degradation with Al doped ZnO and its impact on photocatalytic degradation efficiency. Parameters such as effect of catalyst amount, dye concentration, and pH have been studied. In addition, a possible degradation mechanism is proposed as well.

Materials and methods

All the chemicals used in the present work were of analytical grade (AR), and solutions were prepared in distilled water only. Chemicals used in this work are Zinc Nitrate Hexahydrate (Zn(NO₃)₂·6H₂O), Aluminium Nitrate Nonahydrate (Al(NO₃)₃·9H₂O), and glycine (C₂H₅NO₂). indigo carmine (IC) and azocarmine G (AcG) dyes were used as model pollutants for the photodegradation study.

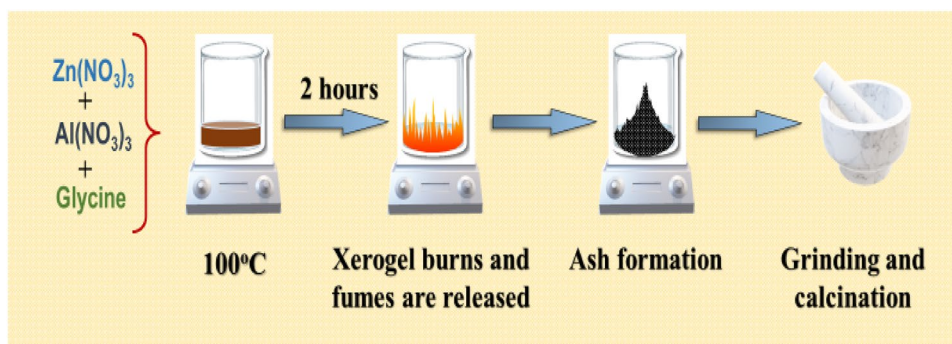
Synthesis of photocatalyst

The nanostructured ZnO and Aluminium doped ZnO (hereafter denoted as AZO, where AZO-2 and AZO-4 denotes ZnO with 2 and 4% Al doping, respectively) nanoparticles were prepared according to previous reports (Prasad et al. 2019). The synthesis was carried out by dissolving Zinc Nitrate Hexahydrate ($\text{Zn}(\text{NO}_3)_2 \cdot 6\text{H}_2\text{O}$), Aluminium Nitrate Nonahydrate ($\text{Al}(\text{NO}_3)_3 \cdot 9\text{H}_2\text{O}$), and Glycine ($\text{NH}_2\text{CH}_2\text{COOH}$) in definite proportions in separate 100 mL of de-ionized water. The metal-to-salt ratio was maintained at 1:2. The mixture was stirred for 10 min on a magnetic stirrer. The mixture was then transferred to a 5 L borosil jar that was kept on a hot plate set at 100 °C. As the time progressed, the excess water evaporated, and the mixture turned into form a xerogel that auto combusted after 2 h of heating. The auto combustion resulted in a fluffy mass that was later ground and calcined at 600 °C for 6 h. The schematic illustration for the synthesis procedure is given in Fig. 1.

Characterizations

X-Ray diffraction was performed on the sample to understand the structure of the synthesized sample. All the diffraction patterns were prepared as step scans with a step size of 0.1° using a monochromatized X-ray beam with Cu-K α ($\lambda = 1.54178 \text{ \AA}$) by X'PERT-Pro MPD, PANalytical Co., Almelo, Netherlands. Raman spectroscopy (Thermo Fisher Scientific DXR Raman Microscope) was used to identify the vibrational modes present in the catalyst. Data from UV–Vis DRS spectrophotometer (Shimadzu UV 3600) in the range 200 to 900 nm was used to calculate bandgap. Photoluminescence (PL) emission studies were performed to study the emission properties of the catalyst (FluoroMax-4, Horiba). Transmission Electron Microscopy (TEM) images were obtained using TECNAI G2 TF20 and Scanning Electron Micrographs (SEM) were obtained using Nove Nano SEM to understand the sample's morphology.

Fig. 1 Schematic illustration of synthesis of AZO nanoparticles using glycine nitrate auto-combustion method



Results and discussions

XRD

Figure 2 shows the powder XRD pattern of the ZnO and AZO nanostructures synthesized by auto combustion technique that were calcined at 600 °C for 6 h. The narrow peak at (100) suggests a good degree of crystallinity of the synthesized nanoparticles. The reflections observed resembled a hexagonal wurtzite-like structure of ZnO that belonged to a space group of P63mc in the Hermann–Mauguin notation with a space group number 186 (JCPDS # 36–1451).

It can be seen from Fig. 2 that an increase in dopant concentration shifts the diffraction angle to higher values, implying that the crystal structure is under stress due to the substitution of Zn^{2+} ions for Al^{3+} ions in the crystalline structure (Mohammadzadeh et al. 2015). It can be concluded from the peak intensity that the crystallinity of the AZO-4 sample is more than the AZO-2. The strain introduced in the

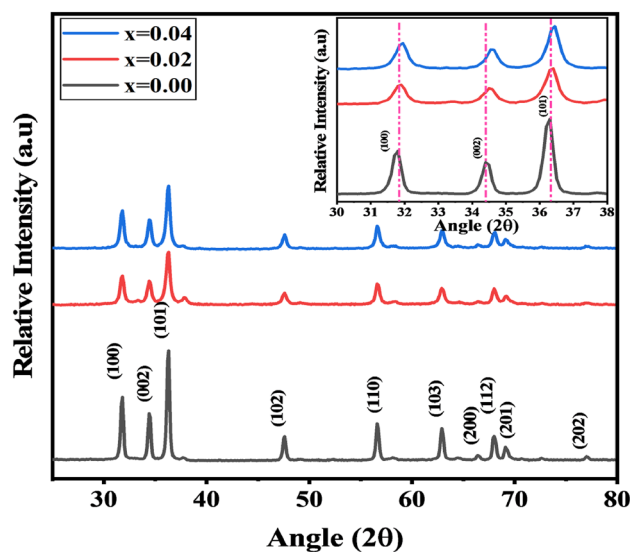


Fig. 2 Room temperature XRD of ZnO and AZO synthesized by auto combustion technique

structure tends to increase with increasing dopant concentrations, owing to the difference in the radii of Al^{3+} and Zn^{2+} . Since the radius of Al^{3+} is 0.53 \AA and that of Zn^{2+} is 0.74 \AA , the doping leads to strain formation in the crystal lattice (Kuo et al. 2006; Karunakaran et al. 2011).

The average crystallite size of the synthesized material was calculated using the standard Debye Scherrer formula $D = 0.9\lambda/\beta \cos \theta$, where D is the crystallite size, β is full-width half maxima and λ is the wavelength of X-rays used. The lattice parameters (' a ' and ' c '), c/a ratio, the volume of the unit cell (V), bond length (L), dislocation density (S) and strain-induced (ϵ) in the matrix for all the materials have been calculated directly from the PowderCell software as shown in the table below. AZO-4 had the smallest crystallite size and the highest strain value. The increase in Al doping was directly proportional to the lattice strain induced in the structure. It has been reported that increasing lattice strain is beneficial for photocatalytic activity (Naldoni et al. 2019). Dislocation density is calculated as $S = 1/D^2$ where D is the crystallite size, and Volume is calculated using Eq. (1):

$$V = \frac{\sqrt{3}}{2} a^2 c \quad (1)$$

Also, the bond length is calculated using Eq. (2):

$$L = \sqrt{\frac{a^2}{3} + \left(\frac{1}{2} - u\right)^2 c^2} \quad (2)$$

where u is the positional parameter given by Eq. (3):

$$u = \frac{a^2}{3c^2} + 0.25 \quad (3)$$

The strain-induced due to crystal imperfection and distortion is calculated using Eq. (4):

$$\epsilon = \frac{\beta_{hkl}}{4 \tan \theta} \quad (4)$$

Table 1 shows the values of all obtained parameters calculated using PowderCell software.

UV-Vis

UV-Vis was used to investigate synthesized ZnO's and AZO's optical properties. It exhibited broad and strong absorption near 364 nm, corresponding to ZnO's

characteristic ground excitonic state. However, the incorporation of Aluminium results in a slight blue shift in absorption for the AZO samples. Band gap of the synthesized catalysts was calculated using Tau'c plot method. The Tau'c method is defined by Eq. (5):

$$\alpha h\nu = (h\nu - E_g)^n \quad (5)$$

where α is the absorption coefficient, h is planks constant, ν is the photon frequency, E_g is the optical bandgap, and $n = 1/2, 2, 3/2$ and 3 for direct allowed, indirect allowed, direct forbidden and indirect forbidden transitions respectively. The intercept to the energy axis gives the optical band gap when extrapolating the straight-line part of the curve, as shown in Fig. 3.

For AZO-4 with increased dopant amount, growth or aggregation of nanoparticles takes place and peak shift was observed. For AZO samples, the optical band gap decreased from 3.02 to 2.96 eV, which is in well accordance with previous literatures (Islam et al. 2019; Bacaksiz et al. 2010; Speaks 2020). Since Zn has higher electronegativity than Al, the band gap may have narrowed after Al doping. After incorporation of Al^{3+} , this difference in electronegativity creates defect sites in the AZO (Rajendran et al. 2016).

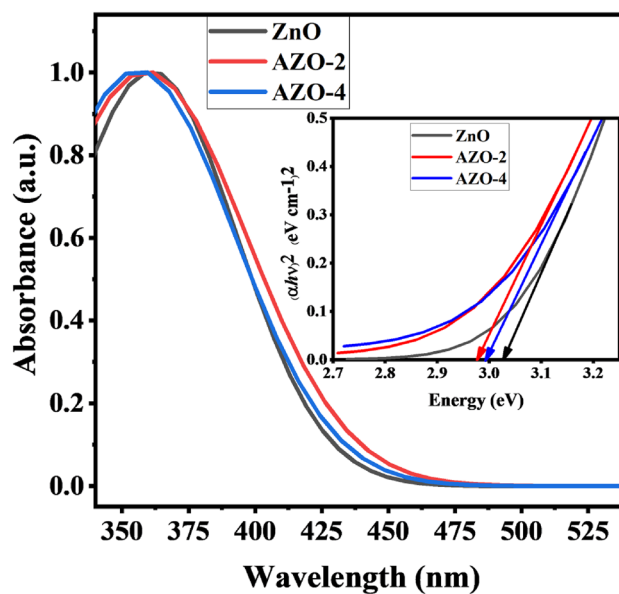


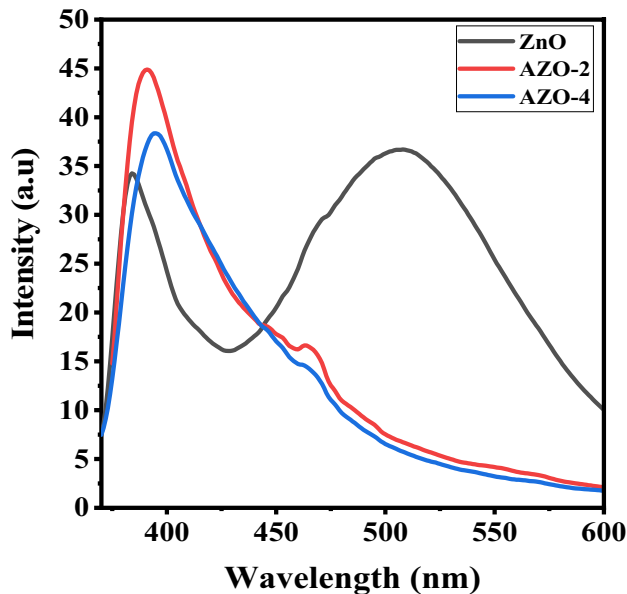
Fig. 3 Absorption spectrum of ZnO and AZO synthesized by auto combustion (Inset: Tau'c pot for band gap calculation)

Table 1 Structural parameters of the synthesized nanoparticles

Catalyst	a (Å)	c (Å)	c/a	V (Å ³)	D (nm)	L (Å)	S	ϵ
ZnO	3.2456	5.1985	1.601707	47.42405	18.54	1.975071	0.00308	0.036934
AZO-2	3.2477	5.2026	1.601934	47.52289	20.54	1.976437	0.00237	0.174124
AZO-4	3.2406	5.1902	1.601617	47.20256	10.35	1.971993	0.00932	0.352107

Table 2 Band gap variation in the catalysts

Al (at %)	E _g (eV)
0	3.02
2	2.96
4	2.99

**Fig. 4** Room temperature emission spectrum of ZnO and AZO catalysts

These defect sites form extended defect levels, causing the conduction band to shift downward and the valence band to shift upward, resulting in a narrowing of the band gap (Vijayalakshmi and Sivaraj 2015). However, the band gap again increased to 2.99 eV for AZO-4, which can be attributed to smaller crystallite size obtained for AZO-4. There are similar reports suggesting relation between crystallite size and band gap (Adesoye et al. 2022; Mouzaia et al. 2020). It may also be possible because dopant segregated in the grain boundary region, inducing impurity levels in the ZnO band structure as reported previously (Venkatachalam et al. 2008; Safeen et al. 2022). In literature, the sample with a larger bandgap has been reported to exhibit a narrow band tail (Dhanaraj et al. 2020; Elsayed et al. 2020). The variations in the band gap for different Al doping are summarized in Table 2.

PL

Emission spectroscopy is an effective method for detecting surface defects in nanomaterials. Figure 4 shows the room temperature photoluminescence (PL) spectra of ZnO and

AZO nanoparticles recorded using excitation wavelength of 360 nm and in the wavelength range of 375–600 nm.

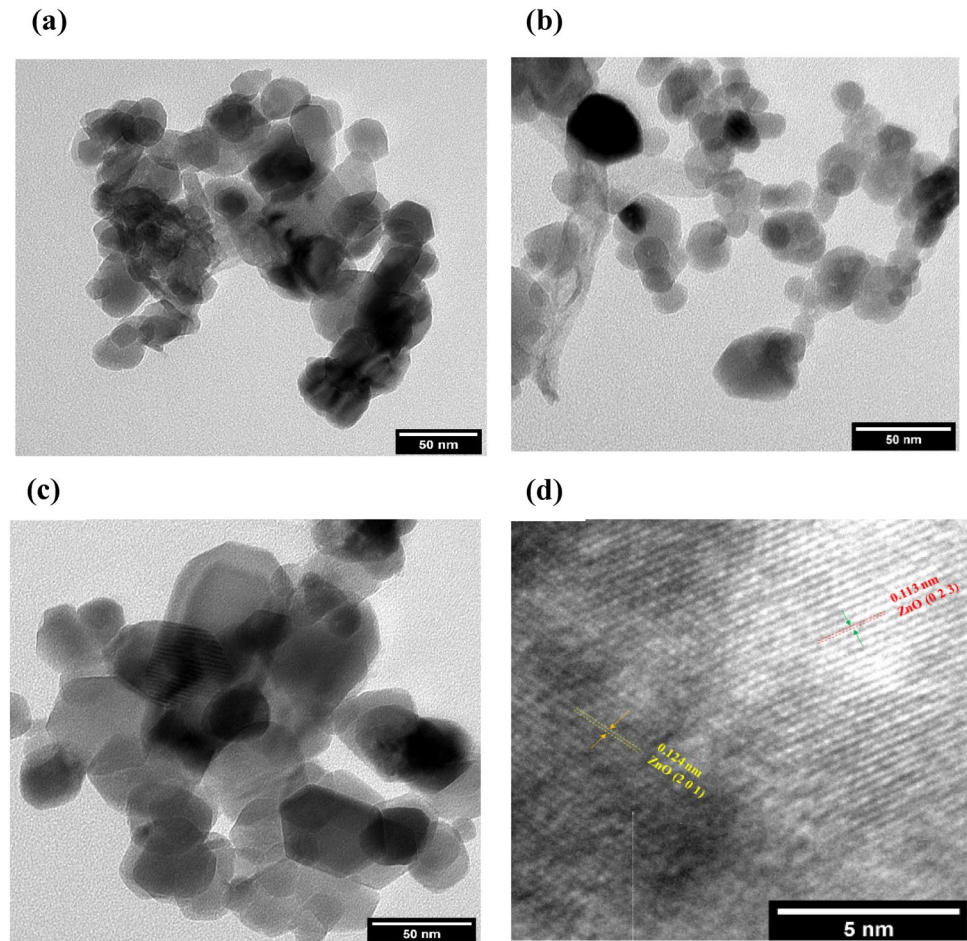
The ZnO photoluminescence spectrum is well known for its ultraviolet (400 nm) and visible emission (blue, green, and yellow emissions in the 400–650 nm range) (Wang et al. 2014). Three emission peaks were observed for all three catalysts around 390 nm, 464 nm, and 566 nm. The UV emission peak around 390 nm generally originates from the recombination of free excitons through excitation-excitation collision process from the valence band to the conduction band (Chai et al. 2014; Wang and Xu 2012). The increased doping amount observed a redshift of UV emission peak. As the amount of doping increased, the intensity of visible emission decreased, indicating that the photoexcited electron is trapped in one of the many impurity levels in the lattice rather than recombining with the hole by emitting a photon. The blue emission band around 460 nm can be ascribed to the transition of an electron from the interstitial Zn_i level below the conduction band to the valence band or singly ionized oxygen vacancies (Bylsma et al. 1986; Kayaci et al. 2014; Yadav et al. 2010). The broad green emission is generally attributed to various intrinsic defects, such as oxygen or zinc vacancy, interstitial oxygen or interstitial zinc or oxygen antisite (Dhayagude et al. 2017). The shoulder at 566 nm is particularly attributed to the recombination of photogenerated holes with singly ionized oxygen vacancies (Gao et al. 2011; Ntwaeaborwa et al. 2017). Because of these excess oxygen vacancies, ZnO has demonstrated excellent photocatalytic activity and gas sensitivity as reported by Yuan et al. (Yuan et al. 2009); hence we believe this is the primary reason for the enhanced photocatalytic ability of AZO-4. In literature, it has already been observed that the reduction in broad emission in the visible region results in a decreased recombination rate of photogenerated electron–hole pairs, hence increasing the photocatalytic activity of the material (Dhayagude et al. 2017; Bhapkar et al. 2023; Ai et al. 2013; Lee et al. 2015).

TEM

Detailed morphologic and structural characterizations of ZnO and AZO photocatalysts were investigated by transmission electron micrographs (TEM). TEM micrographs were obtained at 50 nm resolution.

The synthesized nanoparticles were observed to have quasi-spherical shapes and some elliptical geometries. All the images show aggregation of nanoparticles, which are closely bound to each other. The average particle size was around 25.50 for ZnO, 17.40 nm for AZO-2 and 24.18 nm for AZO-4, as calculated from TEM images using ImageJ software (Fig. 5). The distance between the two adjacent planes, estimated from the lattice fringes, is found

Fig. 5 TEM images of synthesized **a** ZnO, **b** AZO-2, **c** AZO-4, **d** HR-TEM image showing [hkl] planes of ZnO in AZO-4



to be 0.113 nm corresponding to (023) plane spacing and 0.124 nm corresponding to (201) plane spacing of ZnO.

Raman spectroscopy

Raman spectroscopy is an important technique in which sample is interacted with light to probe the defects and impurities. The measurements were performed at room temperature for all the samples and patterns as shown in Fig. 6. A shift in the Raman spectra could be related to the defects (surface impurities or oxygen deficiency) or structural disorder (Shah et al. 2019). The Raman scattering result of synthesized un-doped ZnO nanoparticles was compared with Al-doped ZnO. The fundamental phonon resonance wave numbers reported for ZnO optical modes are E_2 (low) = 100 cm^{-1} , B_{1L} = 273 cm^{-1} , $2E_2$ = 331 cm^{-1} , $A_1(\text{TO})$ = 380 cm^{-1} , E_2 (high) = 440 cm^{-1} and $E_1(\text{LO})$ = 580 cm^{-1} (Tripathy and Kim 2018). The most intense peak is located at approximately 440 cm^{-1} and it is associated with the high frequency branch of ZnO's E_2 (high) mode. This is the characteristic peak for ZnO in the wurtzite crystal structure. This peak is noticed to be shifted to lower wavenumber values of 436 cm^{-1} and 433 cm^{-1} with increase in Al doping is attributed to a lattice distortion caused by the substitution of Al^{3+} with Zn^{2+}

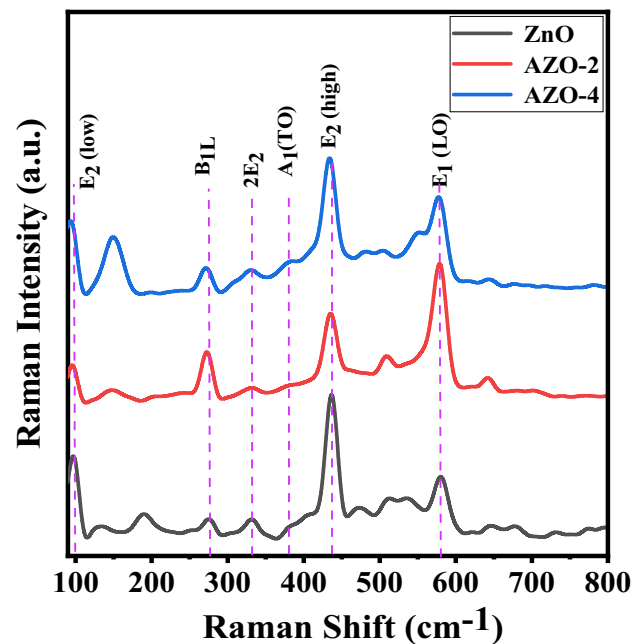


Fig. 6 Raman spectra of ZnO and AZO catalysts

in the ZnO lattice (Efafi et al. 2014). The Al doping in the ZnO lattice causes the FWHM increase for the E_2 (high) mode. The mode at 273 cm^{-1} corresponds to the silent B_{1L} mode which is disorder activated raman scattering. This peak, which has been shifted to a lower wavenumber value, can be attributed to intrinsic host lattice defects in ZnO, where the defect has become activated vibrating complex due to Al incorporation (Bundesmann et al. 2003). Peak at 331 cm^{-1} and a small shoulder at 380 cm^{-1} arises due to $2E_2$ and A_1 (TO) modes respectively. The defect formation in ZnO and doped ZnO can be attributed to the peak at 580 cm^{-1} caused by E_1 (LO) mode. Zhang et al. compared the relative intensities of E_2 (high) and E_1 (LO) modes and found that a higher ratio of E_1 (LO)/ E_2 (high) intensities results in the formation of more defects (Zhang et al. 2008).

Photodegradation studies

The photocatalytic activities of the Al-doped ZnO (AZO) were studied by measuring the degradation of indigo carmine (IC) and azocarmine G (AcG) under sunlight irradiation. All of the experiments were carried out between 9 a.m. and 1 p.m. in September, when the average temperature was just above 30 degrees celsius and the UV index for the month was reported to be 9. IC and AcG were chosen as model dyes because they are non-biodegradable organic pollutants. The stock solution was prepared by adding 50 mg of the dyes in 1000 mL of double distilled water. The dye solutions with concentrations of 10, 20, and 30 mg/L were prepared by diluting the stock solution with deionized water. ZnO and AZO photocatalysts were added to 50 mL of these solutions. Before exposing it to solar light, this aqueous solution was magnetically stirred for 20 min in the dark to eliminate the effect of surface adsorption of dyes by the catalyst and to ensure a uniform suspension of the catalyst in the solution. A certain amount of aliquot was extracted using a syringe at a fixed time interval of 20 min and immediately centrifuged so that metal oxide particles settled at the bottom. The residual concentration of dyes in the solution was used to measure the photocatalytic activity of the synthesized catalyst. The degradation efficiency of dyes was measured using spectrophotometric analysis. The absorbance of IC and AcG was measured by using UV–Visible spectrophotometer (Biochrom, Libra). The maximum wavelength of absorbance λ_{max} for IC and AcG is 610 and 540 nm. After irradiation with visible light, the degradation rate was calculated by computing the change in absorbance at the wavelength of maximum absorbance.

The degradation efficiency of the dye is calculated using Eq. (6):

$$\% \text{ Degradation} = \frac{A_0 - A_t}{A_0} \quad (6)$$

where A_0 represents the initial absorbance of dye before irradiation and A_t represents absorbance after irradiation time 't.'

Effect of Al doping on ZnO: degradation, mechanism

This work studied the photocatalytic activity of ZnO, AZO-2 and AZO-4 on the photodegradation of industrial dyes, namely indigo carmine (IC) and azo carmine G (AcG). With increasing doping concentration, the optical band gap was found to be decreased from 3.02 to 2.96 eV. Such a narrowing in the band gap after adding Al may be attributed to Zn's higher electronegativity than Al's. This difference in electronegativity creates defects sites in the ZnO due to incorporating Al^{3+} (Islam et al. 2019). These defect sites form extended defect levels, which results in band gap narrowing by shifting the valance band upward and the conduction band downward. This band gap narrowing causes more charge carriers to take part in the photocatalytic reaction, improving photocatalytic efficiency.

The effect of Al doping on the degradation of IC and AcG was studied using an invariable dosage of undoped ZnO, along with AZO-2 and AZO-4. The catalyst load was kept at 0.15 g/L, and dye concentrations were 10 ppm. The results showed an increase in photodegradation ability with increased doping. In the case of IC, the degradation rate achieved with ZnO was ~46% after 140 min, whereas for AZO-4, ~97% of IC dye was degraded. AZO-2 was able to degrade ~65 of IC at the same time. For AcG, ZnO degraded ~69%, whereas AZO-2 and AZO-4 degraded ~75 and ~99% of AcG, respectively. This enhancement in the peak reduction was attributed to the reduced band gap of the doped catalyst and incorporation of Al providing the trap states, resulting in reduced e^- and h^+ recombination rate. Figure 7a and b show the obtained results for the variation in Al doping on the degradation of IC and AcG respectively. Table 3 shows the % degradation of IC and AcG obtained by considering change in area under the curve for ZnO and AZO catalysts.

Effect of operating parameters on the degradation of dyes

Catalyst loading

The effect of catalyst dose on the efficiency of dye degradation was studied by varying the AZO-4 catalyst dosage from 0.10 to 0.20 g/L by keeping the concentration of dyes constant at 10 ppm. Results showed that the photodegradation of both the dyes was considerably influenced by photocatalyst dose. The photocatalytic activity significantly increased with increasing catalyst loading, and the optimum dye degradation performance was achieved with a 0.15 g/L catalyst loading. The catalyst loading of 0.1 g/L resulted in ~88% degradation of both IC and AcG dyes. The maximum degradation of ~97% was obtained with 0.15 g/L AZO-4 dosage for IC, and the same amount of catalyst resulted in ~93% degradation of AcG dye.

Further increase in dosage amount negatively impacted the degradation of both the dyes, where IC and AcG could be

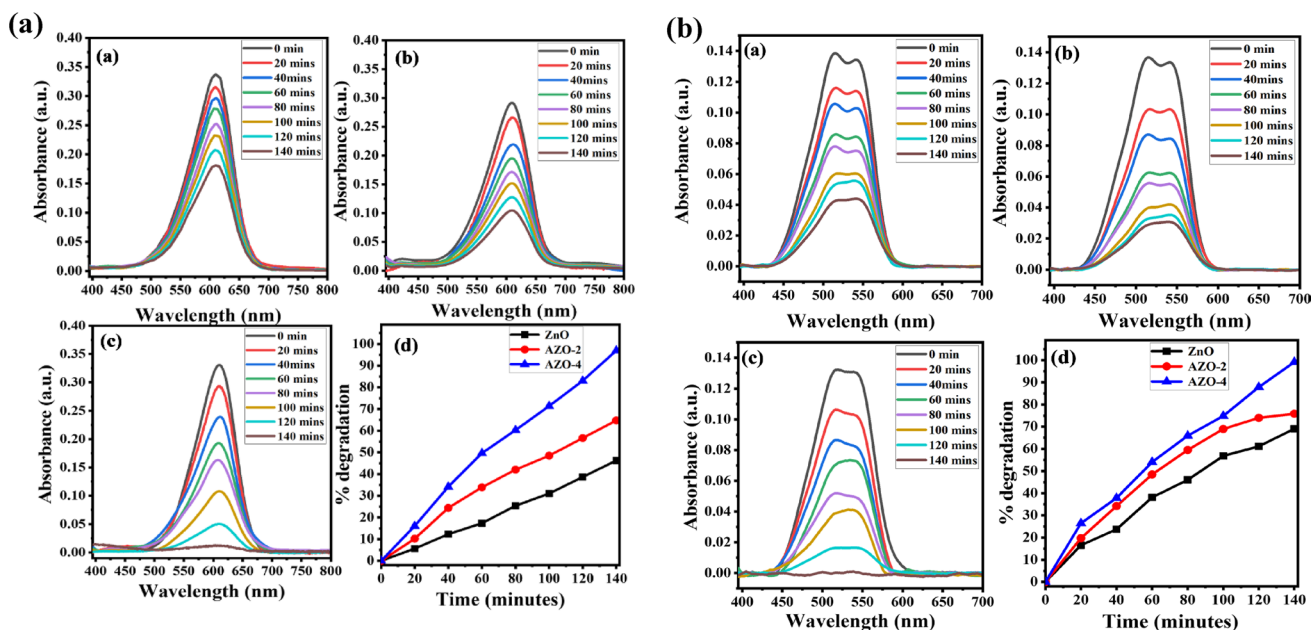


Fig. 7 a The degradation of IC by a ZnO, b AZO-2, c AZO-4, d degradation efficiency. b The degradation of AcG by a ZnO, b AZO-2, c AZO-4, d degradation efficiency

Table 3 Effect of Al doping: degradation calculated using area under the curve

Catalyst	% degradation using area under the curve for IC	% degradation using area under the curve for AC
ZnO	44.44	68.13
AZO-2	65.15	77.88
AZO-4	91.35	98.21

degraded to ~84 and ~75%, respectively. Suppose an adequate amount increases the catalyst load. In that case, more active sites will enhance the generation of electron–hole pairs and, thus, the formation of hydroxyl radicals and superoxide anions responsible for increased photodegradation efficiency (Rajput et al. 2022). On the other hand, increased catalyst loading harmed the photocatalytic efficiency and caused the degradation rate constant to decrease. This can be explained by the fact that the catalyst particles undergo particle–particle interaction producing a screening effect, which prevents photons from reaching the photocatalyst surface, decreasing photodegradation efficiency (Nguyen et al. 2022; Kalita et al. 2022). Figure 8a, b show the obtained results for the variation in catalyst loading on the degradation of IC and AcG using AZO-4 as a photocatalyst. Table 4 shows the % degradation of IC and AcG obtained by considering change in area under the curve for varying AZO-4 loading.

Dye concentration

To investigate the effect of initial dye concentration on the degradation of IC and AcG, dye concentrations were varied

from 10 to 30 ppm with constant AZO-4 loading of 0.15 g/L. Figure 9 shows the effect of initial dye concentration on degradation of IC and AcG. It was found that the % degradation was inversely proportional to dye concentration. At an initial concentration of 10 ppm with 0.15 g/L AZO-4 loading, the maximum degradation of 96.67% was obtained, while at an initial concentration of 30 ppm, the degradation was minimum at 24.27% for IC. Similar results were obtained in the case of AcG, with maximum degradation at 10 ppm being 99%, which then decreases to 69% for 30 ppm. According to the literature, at lower dye concentrations, the oxidizing radicals are in excess, oxidizing a greater amount of dye available in the solution and resulting in maximum dye degradation (Neppolian et al. 2002; Fereidooni et al. 2022). However, the availability of oxidizing species decreases as dye concentrations exceed the optimal level, resulting in less degradation (Bagal et al. 2022). In the case of AZO-4 particles, as the quantity of contaminant molecules near the catalyst surface rises as dye concentrations rise, additional reactive species ($HO\cdot$ and $O_2\cdot^-$) are needed. Due to the limited number of active sites, the amount of oxidizing agents in the solution is insufficient to absorb $HO\cdot$ and $O_2\cdot^-$ molecules. As a result, increasing the dye's initial concentration reduces the possibility of dye molecules interacting with oxidizing species. It is worth noting that intermediates formed during the process may cause side reactions and absorb free radicals in the solution (such as $HO\cdot$ radicals). As the dye concentration increased, the competition for free radicals between dye molecules and intermediates reduces process efficiency, which leads to lower degradation efficiency. Table 5 shows the %

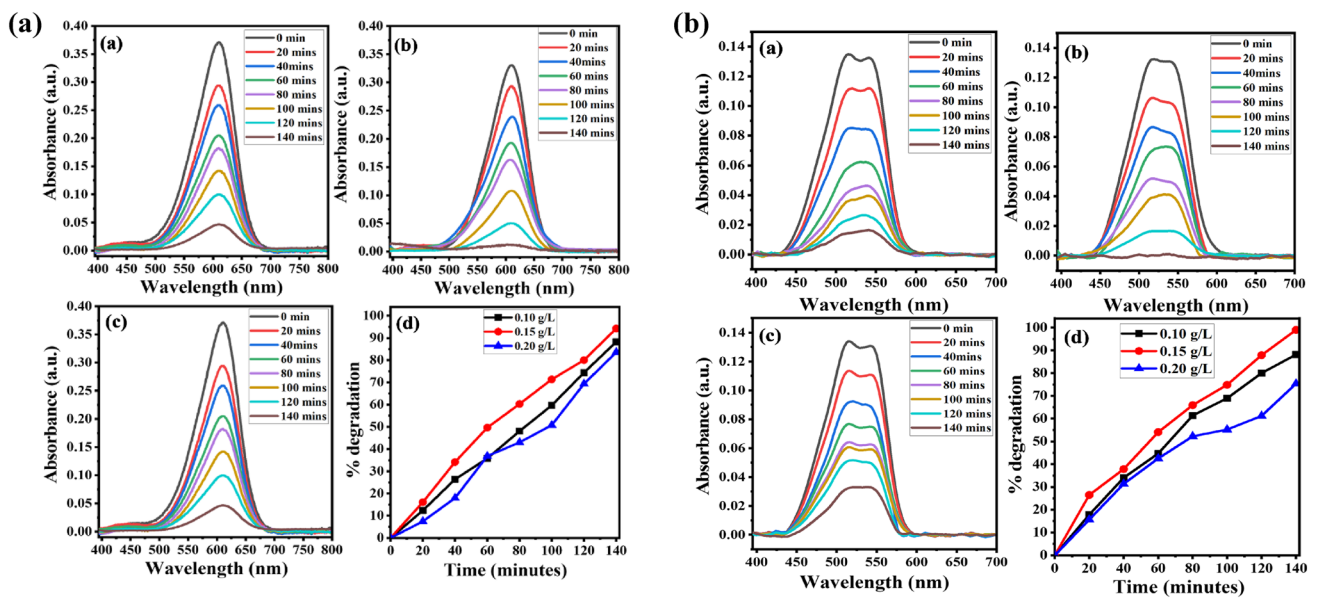


Fig. 8 a The effect of catalyst loading on the degradation of IC by AZO-4, a 0.1 g/L, b 0.15 g/L, c 0.2 g/L, d degradation efficiency. b The effect of catalyst loading on the degradation of AcG by AZO-4, a 0.1 g/L, b 0.15 g/L, c 0.2 g/L, d degradation efficiency

Table 4 Effect of catalyst loading: degradation calculated using area under the curve

Catalyst loading g/L	% degradation using area under the curve for IC	% degradation using area under the curve for AcG
0.1	86.05	89.16
0.15	91.35	98.21
0.2	80.11	77.62

degradation of IC and AcG obtained by considering change in area under the curve for varying initial dye concentrations.

pH effect

pH is an important parameter in photocatalytic dye decolorization since it affects dye reaction rates in a variety of ways. Because catalyst surface charge is affected by the pH of a solution, pH can influence dye adsorption on the

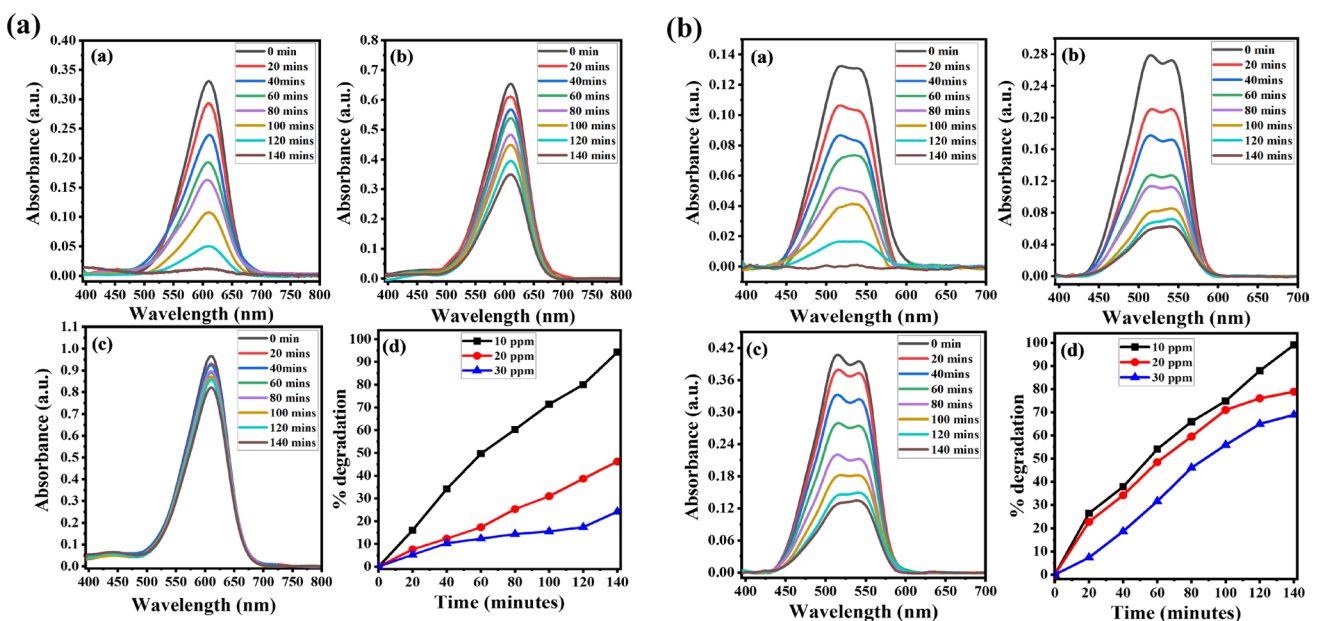


Fig. 9 a The effect of IC dye concentration on the degradation by AZO-4, a 10 ppm, b 20 ppm, c 30 ppm, d degradation efficiency. b The effect of AcG dye concentration on the degradation by AZO-4, a 10 ppm, b 20 ppm, c 30 ppm, d degradation efficiency

Table 5 Effect of dye concentration: degradation % calculated using area under the curve

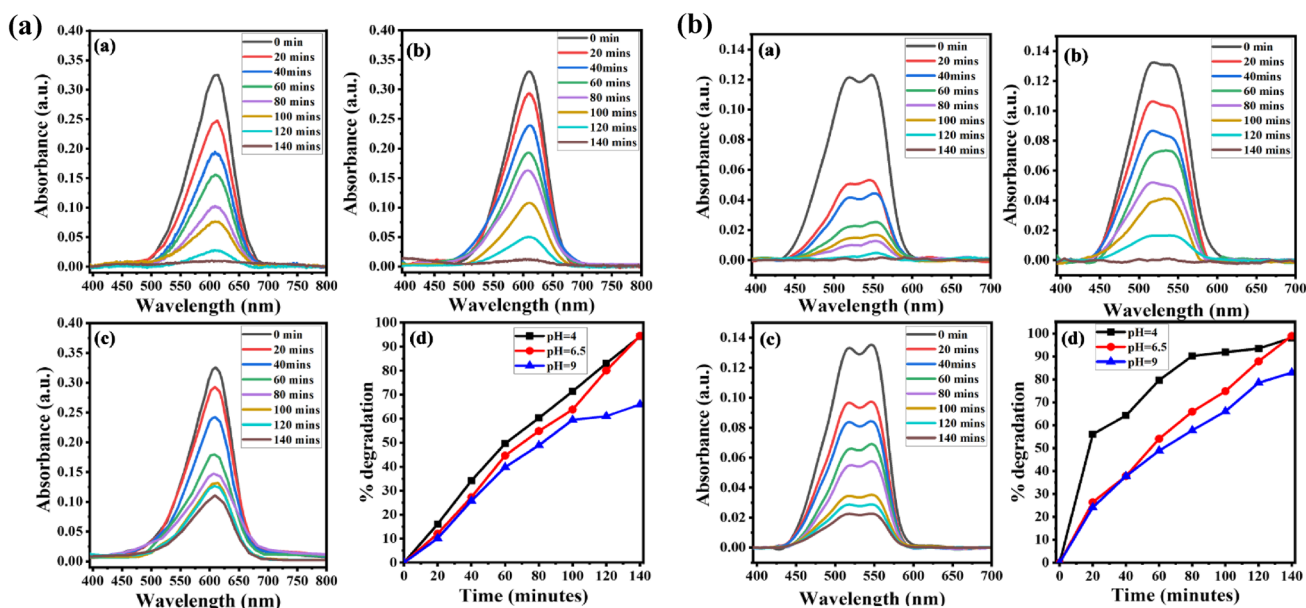
Dye concentration (ppm)	% degradation using area under the curve for IC	% degradation using area under the curve for AcG
10	91.35	98.21
20	47.08	77.85
30	21.12	67.94

semiconductor's surface and also the generation of hydroxyl radicals (Anne et al. 2002; Paul et al. 2019). Two factors stand out when studying the effect of pH on photocatalytic dye degradation. One, industrial pollutants may not be neutral. Second, the pH of the reaction mixture influences the photocatalysts' surface-charge properties (Chakrabarti and Dutta 2004). The effect of pH on the photocatalytic performance is explained by electrostatic forces between the catalyst and dye. Dye degradation is maximum around the point of zero charges (pHpzc), estimated at ~pH 7 using the previously reported method. Means at this pH, the catalyst's surface is neutral or has no charge (Yang et al. 2004; Zhu et al. 2012).

At a pH lower than 7, the surface of the photocatalyst is positively charged, resulting in cation repelling/anion attracting. At a pH higher than 7, the surface attains a negative charge due to the absorption of hydroxyl ions, and the surface becomes anion-repelling/cation-attracting (Rafiq et al. 2021). Since IC and AcG both are anionic dyes, their negative ions will get adsorbed on a positive

surface of the catalyst, achieved at pH below 7, resulting in improved degradation of both dyes under neutral to acidic conditions. However, at pH 9, the anions of the dye interact with the negative surface of the catalyst, which results in coulombic repulsion between the dye and catalyst, resulting in reduced degradation efficiency of IC and AcG under basic conditions.

The degradation studies were carried out at three different pH values of 4, 6.5 and 9 and by keeping a constant catalyst load at 0.15 g/L and dye concentration at 10 ppm. Figure 10 shows the effect of pH on degradation of IC and AcG. The results show that increasing the pH value decreases the rate of degradation and photocatalyst efficiency. In the case of IC, at acidic pH of 4, the degradation rate was found to be ~97% after 140 min. At the pH of double distilled water (6.5), ~97% dye was degraded, while pH 9 resulted in ~65% degradation in 140 min. The degradation obtained after 60 min for pH 4, 6.5 and 9 were 50%, 48% and 39%, respectively. For AcG, at acidic pH of 4, the degradation rate was ~98% after 140 min, whereas ~99% and ~83% degradation was obtained at pH 6.5 and 9 respectively. The degradation obtained after 60 min for pH 4, 6.5 and 9 were 79%, 54% and 49%, respectively. Hence, it can be concluded that the degradation rate of anionic dyes is faster in an acidic medium and AZO-4 was efficient in the degradation of dyes in neutral as well as acidic conditions. Table 6 shows the % degradation of IC and AcG obtained by considering change in area under the curve for varying pH values.

**Fig. 10** a The effect of pH on the degradation of IC at pH values a 4, b 6.5, c 9, d degradation efficiency. b The effect of pH on the degradation of AcG at pH values a 4, b 6.5, c 9, d degradation efficiency

Reaction kinetics

To estimate the photocatalytic reactivity of the samples regarding degradation of IC and AcG, a pseudo-first-order kinetic model was tested for optimized parameters with 0.15 g/L catalyst loading and 10 ppm dye concentration for all 3 catalysts. From the R^2 values, the reactions were found to be following first-order kinetics, which is generally expressed by Eq. (7).

$$\ln\left(\frac{A_0}{A_t}\right) = kt \tag{7}$$

Where A_0 is the initial absorbance of dye, A_t is absorbance after time ‘t’, and the slope of the $\ln(A_0/A_t)$ vs. time plot gives the value of ‘k’, which is the rate constant (min^{-1}) for the reaction. The higher value of ‘k’ corresponds to better photocatalytic activity (Dong et al. 2017). The results in Table 7 can be used to deduce two facts: The first is ZnO’s low photocatalytic activity, which can be attributed to faster electron–hole recombination; the second is increased photocatalytic activity of Al doped ZnO, that can be attributed to the transfer of photogenerated electrons from the ZnO’s CB to Al trap sites, which limits electron–hole recombination (Mendoza-Mendoza et al. 2018; Kadam et al. 2018). Figure 11 shows the first-order kinetic curves for the degradation of IC and AcG using ZnO and AZO catalysts.

Table 6 Effect of pH: degradation % calculated using area under the curve

pH	% degradation using area under the curve for IC	% degradation using area under the curve for AcG
4	92.86	99.37
6.5	91.35	98.21
9	63.52	82.74

The photodegradation activity of photocatalysts regarding rate constant (k) and linear regression coefficient (R^2) have been studied with both IC and AcG dyes. The values of k and R^2 are summarized in Table 7.

Mixed dye effect

To check the effectiveness of the AZO-4 on the mixture of dyes, degradation experiments were performed by taking a mixture of both dyes with the optimized catalyst loading of 0.15 g/L. Since, on an industrial level, the discarded wastewater may contain a mixture of the dyes, we wanted to explore this new idea of mixing the dyes and checking its effect on degradation. Complete degradation was obtained with the dye mixture, proving the effectiveness of synthesized photocatalysts. Figure 12 shows the absorbance spectra and degradation efficiency of dye mixture by using AZO-4 catalyst.

It is worth noting that the absorbance value after mixing the dyes changed concerning both dyes, while the wavelength of maximum absorbance coincided with that of the IC. It can be suggested that after mixing the dyes, they did not chemically react with each other but formed a uniform suspension.

Table 7 Summary of pseudo-first-order rate kinetics for the degradation of IC and AcG

Catalyst	Indigo carmine		Azocarmine G	
	Rate constant k (min^{-1})	Linear regression coefficient (R^2)	Rate constant k (min^{-1})	Linear regression coefficient (R^2)
ZnO	0.00436	0.99078	0.00826	0.99413
AZO 2	0.00727	0.99413	0.01136	0.99069
AZO 4	0.01836	0.98165	0.01833	0.95478

Fig. 11 The first-order reaction kinetics of ZnO and AZO for the degradation of **a** Indigo Carmine **b** Azocarmine G

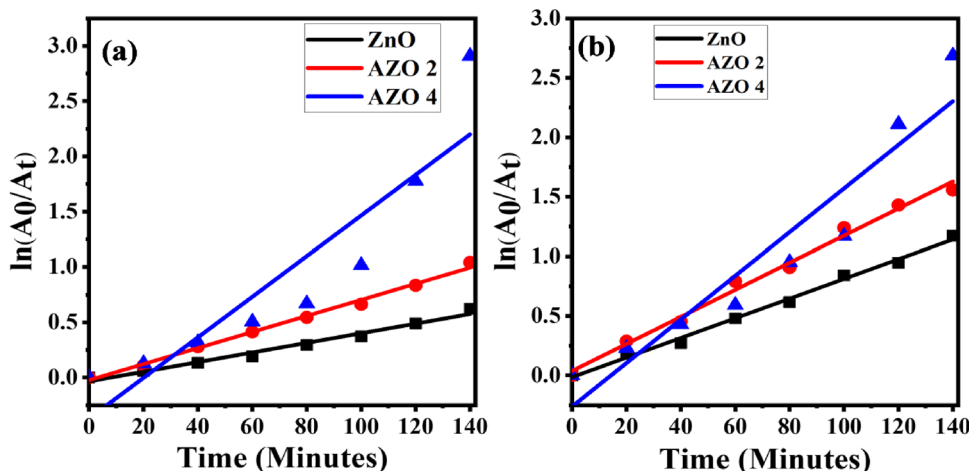
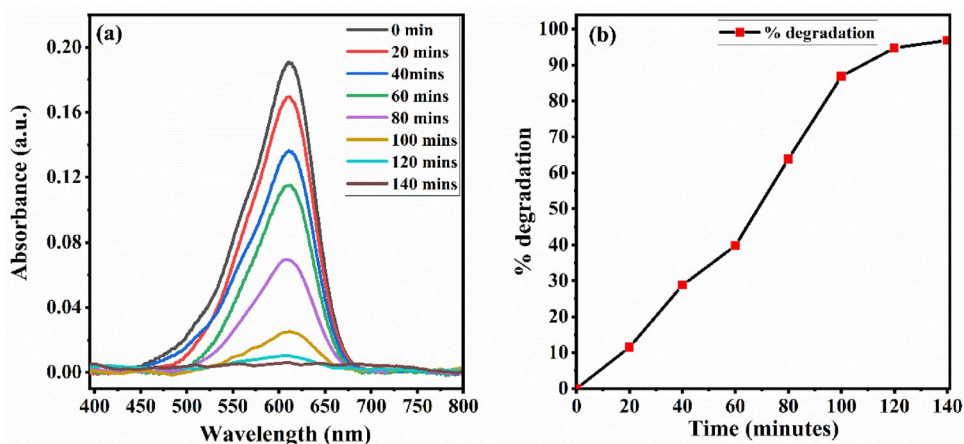
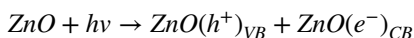


Fig. 12 The effect of the mixture of dyes **a** absorbance spectra, **b** degradation efficiency

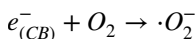
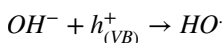
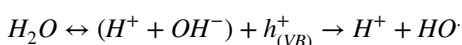


Degradation mechanism

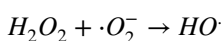
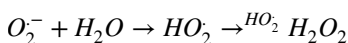
When the photons of energy more than or equal to the band gap of the photocatalyst incident on it, the electrons (e^-) in the valence band get excited, and they move to the conduction band, leaving behind a hole (h^+) in the valence band.



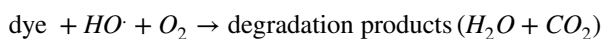
where $h\nu$ is the energy required to transfer the electron from the valence band to the conduction band. The valence band undergoes an oxidation reaction where photo-induced holes can get trapped by H_2O molecules or surface hydroxyl groups on the photocatalyst resulting in the production of hydroxyl radicals (Sohrabnezhad and Seifi 2016). At the same time, the reduction reaction occurs at the conduction band, where electrons react with oxygen molecules in the vicinity of the reaction atmosphere, producing superoxide anions (Han et al. 2012). It can be written as:



These superoxide radicals subsequently react with H_2O molecules to produce hydroperoxyl radical (HO_2^\cdot). Two hydroperoxyl radicals combine to form hydrogen peroxide H_2O_2 which then converts to hydroxyl radical, a strong oxidizing agent responsible for the degradation of dye (Jongnavakit et al. 2012). The reaction can be written as follows:



Finally, dye molecules will get oxidized to yield carbon dioxide and water as follows:



The mechanism for the photocatalytic degradation by AZO photocatalyst under solar irradiation is shown in Fig. 13.

The photo-excited electrons in the conduction band are very unstable. They easily return to the valence band and recombine with the hole. This reduces the photocatalytic reaction's quantum yield. Metal doping can improve photocatalytic efficiency by reducing the charge carrier recombination rate. Dopant atoms act as charge traps by creating localized electronic states for the photogenerated charge carrier, enhancing the mean lifetime (Park et al. 2015). The trapped charges transfer to the catalyst's surface and react with the dye molecules increasing photocatalytic efficiency by suppressing the electron–hole recombination. The findings of this study are compared with previous works on the degradation of indigo carmine and azocarmine G and brief summary is given in the Table 8.

Conclusion

ZnO and Al-doped ZnO nanoparticles with wurtzite hexagonal structure were successfully synthesized by Glycine-Nitrate auto-combustion route and synthesized catalysts showed extraordinary photocatalytic performance in the degradation of indigo carmine and azocarmine G dyes under sunlight. The crystallite size was between 10 and 20 nm, as calculated from XRD data. UV–VIS spectra revealed that the bandgap of synthesized nanoparticles varied between 2.96 and 3.02 eV. The enhanced photo-degradation performance can be attributed to the reduction in crystallite size, band gap, as well as presence of excess oxygen vacancies and Zn interstitial sites in the

Fig. 13 Schematic design of dye degradation using AZO as photocatalyst

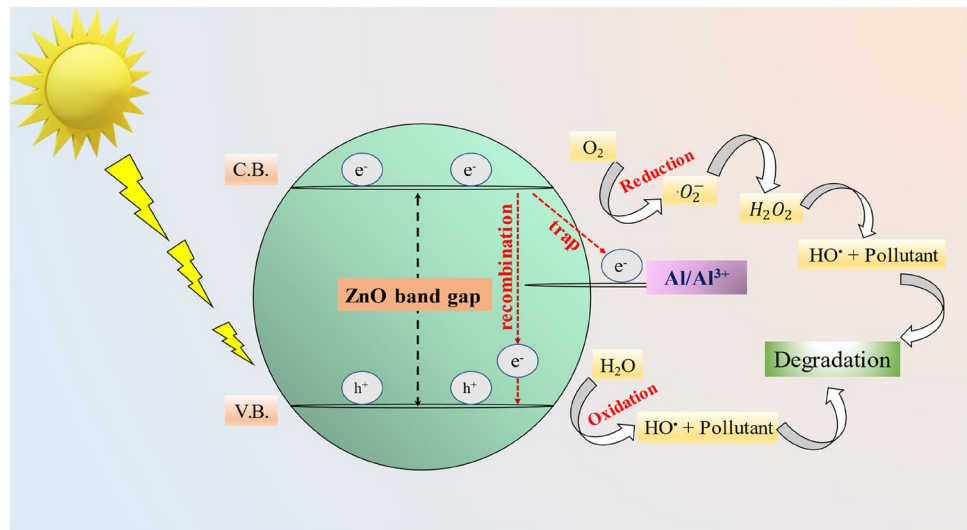


Table 8 Comparison of experimental conditions for the degradation of indigo carmine and azocarmine G in several works

Catalyst	Dye	Dosage (g/L)	Source	Synthesis technique	Dye conc. (ppm)	Exposure time (min)	% Degradation	References
ZnO-Al (4%)	IC	0.15	Sunlight	Glycine nitrate	10	140	97	This work
CA-CNT/TiO ₂	IC	–	UV	Electrospinning	10	180	99	Salama et al. (2018)
CoFe ₂ O ₄ /SnO ₂	IC	0.1	UV	Sonochemical	20	120	55	Abouseada et al. (2022)
Ag/ZnO	IC	1.0	Vis	Coprecipitation	10	120	95	Kumar et al. (2022)
ZnO/Zn	IC	–	UV-C	Hydrothermal	2	60	99	Yudasari et al. (2021)
WO ₃ /CeO ₂	IC	2.0	Vis	Coprecipitation	3	120	30	Channei et al. (2021)
ZnO-Al (4%)	AcG	0.15	Sunlight	Glycine nitrate	10	140	99	This work
Polystyrene/ZnO	AcG	0.5	Sunlight	Electrospinning	10	720	95	El-Samak et al. (2022)
PANI-BiYTi ₂ O ₇	AcG	2.0	Vis	Solid state mixing	20	330	97	Luan et al. (2017)

nanoparticles as determined by PL spectroscopy. TEM analysis showed that the synthesized ZnO nanoparticles were quasi-spherical in shape, with particle size averaging between 17 and 25 nm. Photodegradation studies revealed that maximum degradation was observed when dye concentration was 10 ppm and catalyst loading was 0.15 g/L, and degradation achieved was 97 and 99% for indigo carmine and azo carmine G, respectively. The pH of the dye solution was found to be a very effective parameter, resulting in faster degradation in acidic pH for both the dyes. Kinetic studies revealed that photodegradation reactions followed pseudo-first-order kinetics.

Acknowledgements This work was supported by an NPRP grant from the Qatar National Research Fund under NPRP12S-0131–190030. The statements made herein are solely the responsibility of the authors. The authors are indebted to acknowledge the analytical and technical support by Central Laboratories Unit in characterizing TEM samples and are very much thankful to the Central Laboratories Unit. Abhishek Bhapkar is grateful to Symbiosis Centre for Research and Innovation (SCRI) for Junior Research Fellowship.

Funding Open Access funding provided by the Qatar National Library.

Data availability The datasets used and analysed during the current study are available from the corresponding author on reasonable request.

Declarations

Conflict of interest The authors declare that they have no conflict of interest.

Open Access This article is licensed under a Creative Commons Attribution 4.0 International License, which permits use, sharing, adaptation, distribution and reproduction in any medium or format, as long as you give appropriate credit to the original author(s) and the source, provide a link to the Creative Commons licence, and indicate if changes were made. The images or other third party material in this article are included in the article's Creative Commons licence, unless indicated otherwise in a credit line to the material. If material is not included in the article's Creative Commons licence and your intended use is not permitted by statutory regulation or exceeds the permitted use, you will need to obtain permission directly from the copyright holder. To view a copy of this licence, visit <http://creativecommons.org/licenses/by/4.0/>.

References

- Abouseada N, Ahmed MA, Elmahgary MG (2022) Materials science for energy technologies synthesis and characterization of novel magnetic nanoparticles for photocatalytic degradation of indigo carmine dye. *Mater Sci Energy Technol* 5:116–124. <https://doi.org/10.1016/j.mset.2022.01.001>
- Adam RE, Pozina G, Willander M, Nur O (2018) Synthesis of ZnO nanoparticles by co-precipitation method for solar driven photo-degradation of Congo red dye at different pH. *Photonics Nanostr Fundam Appl* 32:11–18. <https://doi.org/10.1016/J.PHOTONICS.2018.08.005>
- Adesoye S, Al Abdullah S, Nowlin K, Dellinger K (2022) Mg-doped ZnO nanoparticles with tunable band gaps for surface-enhanced raman scattering (SERS)-based sensing. *Nanomaterials* 12:3564. <https://doi.org/10.3390/nano12203564>
- Ai L, Zhang C, Meng L (2011) Adsorption of methyl orange from aqueous solution on hydrothermal synthesized Mg–Al layered double hydroxide. *J Chem Eng Data* 56:4217–4225. <https://doi.org/10.1021/je200743u>
- Ai ZW, Wu Y, Wu H, Wang T, Chen C, Xu Y, Liu C (2013) Enhanced band-edge photoluminescence from ZnO-passivated ZnO nanoflowers by atomic layer deposition. *Nanoscale Res Lett* 8:2–7. <https://doi.org/10.1186/1556-276x-8-105>
- Almehizia AA, Al-Omar MA, Naglah AM, Bhat MA, Al-Shakliah NS (2022) Facile synthesis and characterization of ZnO nanoparticles for studying their biological activities and photocatalytic degradation properties toward methylene blue dye. *Alexandria Eng. J.* 61:2386–2395. <https://doi.org/10.1016/j.aej.2021.06.102>
- Bacaksiz E, Aksu S, Salih Y, Parlak M, Altunba M (2010) Structural optical and electrical properties of Al-doped ZnO microrods prepared by spray pyrolysis. *Thin Solid Films* 518:4076–4080. <https://doi.org/10.1016/j.tsf.2009.10.141>
- Bagal M, Kumbhar G, Shukla S, Tiwari A, Gajbhiye D, Mohod A (2022) Degradation of dye in a continuous zig-zag flow pattern photocatalytic reactor using a Doehler matrix. *Chem Eng Res Des* 188:315–329. <https://doi.org/10.1016/J.CHERD.2022.09.019>
- Bai X, Wang L, Zong R, Lv Y, Sun Y, Zhu Y (2013) Performance enhancement of ZnO photocatalyst via synergic effect of surface oxygen defect and graphene hybridization. *Langmuir* 29:3097–3105. <https://doi.org/10.1021/la4001768>
- Balouch A, Jagirani MS, Alveroglu E, Lal S, Sirajuddin, Mahar AM, Mal D (2022) Ultra-fast degradation of thymol blue dye under microwave irradiation technique using alpha-orthorhombic molybdenum trioxide (α -MoO₃) colloidal nanoparticles. *J Clust Sci.* <https://doi.org/10.1007/s10876-022-02381-9>
- Bhapkar A, Prasad R, Jaspal D, Shirolkar M, Gheisari K, Bhame S (2023) Visible light driven photocatalytic degradation of methylene blue by ZnO nanostructures synthesized by glycine nitrate auto combustion route. *Inorg Chem Commun* 148:110311. <https://doi.org/10.1016/J.INOCHE.2022.110311>
- Bhatti MA, Almaani KF, Shah AA, Tahira A, Chandio AD, Mugheri AQ, Bhatti AL, Waryani B, Medany SS, Nafady A, Ibutoto ZH (2022) Low temperature aqueous chemical growth method for the doping of W into ZnO nanostructures and their photocatalytic role in the degradation of methylene blue. *J Clust Sci* 33:1445–1456. <https://doi.org/10.1007/s10876-021-02069-6>
- Bundesmann C, Ashkenov N, Schubert M, Spemann D, Butz T, Kaidashev EM, Lorenz M, Grundmann M (2003) Raman scattering in ZnO thin films doped with Fe, Sb, Al, Ga, and Li. *Appl Phys Lett* 83:1974–1976. <https://doi.org/10.1063/1.1609251>
- Bylsma RB, Becker WM, Kossut J, Debska U, Yoder-Short D (1986) Dependence of energy gap on x and T in Zn_{1-x}Mn_xSe: the role of exchange interaction. *Phys Rev B* 33:8207–8215. <https://doi.org/10.1103/PHYSREVB.33.8207>
- Chai B, Wang X, Cheng S, Zhou H, Zhang F (2014) One-pot triethanolamine-assisted hydrothermal synthesis of Ag/ZnO heterostructure microspheres with enhanced photocatalytic activity. *Ceram Int* 40:429–435. <https://doi.org/10.1016/J.CERAMINT.2013.06.019>
- Chakrabarti S, Dutta BK (2004) Photocatalytic degradation of model textile dyes in wastewater using ZnO as semiconductor catalyst. *J Hazard Mater* 112:269–278. <https://doi.org/10.1016/j.jhazmat.2004.05.013>
- Chandio AD, Pato AH, Channa IA, Gilani SJ, Shah AA, Ashfaq J, Buledi JA, Chandio IA, Bin Jumah MN (2022) Exploring the heterocatalytic proficiencies of ZnO nanostructures in the simultaneous photo-degradation of chlorophenols. *Sustain.* <https://doi.org/10.3390/su142114562>
- Chandraboss VL, Natanapatham L, Karthikeyan B, Kamalakkannan J, Prabha S, Senthilvelan S (2013) Effect of bismuth doping on the ZnO nanocomposite material and study of its photocatalytic activity under UV-light. *Mater Res Bull* 48:3707–3712. <https://doi.org/10.1016/j.materresbull.2013.05.121>
- Chang C-J, Yang T-L, Weng Y-C (2014) Synthesis and characterization of Cr-doped ZnO nanorod-array photocatalysts with improved activity. *J Solid State Chem* 214:101–107. <https://doi.org/10.1016/j.jssc.2013.09.039>
- Chang C-J, Lin C-Y, Hsu M-H (2014) Enhanced photocatalytic activity of Ce-doped ZnO nanorods under UV and visible light. *J Taiwan Inst Chem Eng* 45:1954–1963. <https://doi.org/10.1016/j.jtice.2014.03.008>
- Chaneei D, Chansaenpak K, Phanichphant S, Jannoey P, Khanitchaidecha W, Nakaruk A (2021) Synthesis and characterization of WO₃/CeO₂ Heterostructured nanoparticles for photodegradation of indigo carmine dye. *ACS Omega* 6:19771–19777. <https://doi.org/10.1021/acsomega.1c02453>
- Cheng HH, Chen SS, Liu HM, Jang LW, Chang SY (2020) Glycine-nitrate combustion synthesis of Cu-based nanoparticles for NP9EO degradation applications. *Catalysts* 10:1–13. <https://doi.org/10.3390/catal10091061>
- Daneshvar N, Salari D, Khataee AR (2004) Photocatalytic degradation of azo dye acid red 14 in water on ZnO as an alternative catalyst to TiO₂. *J Photochem Photobiol A Chem* 162:317–322. [https://doi.org/10.1016/S1010-6030\(03\)00378-2](https://doi.org/10.1016/S1010-6030(03)00378-2)
- Davis K, Yarbrough R, Froeschle M, White J, Rathnayake H (2019) Band gap engineered zinc oxide nanostructures via a sol-gel synthesis of solvent driven shape-controlled crystal growth. *RSC Adv.* 9:14638–14648. <https://doi.org/10.1039/c9ra02091h>
- Dhanaraj A, Das K, Keller JM (2020) A study of the optical band gap energy and Urbach energy of fullerene (C 60) doped PMMA nanocomposites. *AIP Conf Proc* 2270:110040. <https://doi.org/10.1063/5.0019420>
- Dhayagude AC, Nikam SV, Kapoor S, Joshi SS (2017) Effect of electrolytic media on the photophysical properties and photocatalytic activity of zinc oxide nanoparticles synthesized by simple electrochemical method. *J Mol Liquids.* 232:290–303. <https://doi.org/10.1016/j.molliq.2017.02.074>
- Dong P, Yang B, Liu C, Xu F, Xi X, Hou G, Shao R (2017) Highly enhanced photocatalytic activity of WO₃ thin films loaded with Pt-Ag bimetallic alloy nanoparticles. *RSC Adv.* 7:947. <https://doi.org/10.1039/c6ra25272a>
- Efafi B, Sasani Ghamsari M, Aberoumand MA, Majles Ara MH, Sasani Ghamsari AH, Hojati Rad H (2014) Aluminum doped ZnO sol-gel derived nanocrystals: Raman spectroscopy and solid solubility characterization. *Phys Status Solidi Appl Mater Sci* 211:2426–2430. <https://doi.org/10.1002/pssa.201431075>
- El-Kammah M, Elkhatib E, Gouveia S, Cameselle C, Aboukila E (2022) Enhanced removal of Indigo Carmine dye from textile

- effluent using green cost-efficient nanomaterial: adsorption, kinetics, thermodynamics and mechanisms. *Sustain Chem Pharm* 29:100753. <https://doi.org/10.1016/j.scp.2022.100753>
- El-Samak AA, Ponnamma D, Hassan MK, Al-Maadeed MAA (2022) A stable porous vessel for photocatalytic degradation of Azocarmine G dye. *Microporous Mesoporous Mater* 341:111994. <https://doi.org/10.1016/j.micromeso.2022.111994>
- Elsayed NM, Farag OF, Elghazaly MH, Nasrallah DA (2020) Investigation of the effects of fullerene addition and plasma exposure on optical properties of polystyrene films. *IOSR J Appl Phys* 7:64–70. <https://doi.org/10.9790/4861-07626470>
- Fereidooni M, Esmailzadeh F, Zandifar A (2022) Innovatively-synthesized CeO₂/ZnO photocatalysts by sono-photochemical deposition: catalyst characterization and effect of operational parameters on high efficient dye removal. *J Mater Sci* 57:16228–16244. <https://doi.org/10.1007/S10853-022-07666-Y/TABLES/9>
- Fox MA, Dulay MT (2002) Heterogeneous photocatalysis. *Chem Rev* 93:341–357. <https://doi.org/10.1021/cr00017a016>
- Fujishima A, Honda K (1972) Electrochemical photolysis of water at a semiconductor electrode. *Nature* 238:37–38. <https://doi.org/10.1038/238037a0>
- Ganesh V, Salem GF, Yahia IS, Yakuphanoglu F (2018) Synthesis, optical and photoluminescence properties of Cu-doped ZnO nano-fibers thin films: nonlinear optics. *J Electron Mater* 47:1798–1805. <https://doi.org/10.1007/s11664-017-5950-6>
- Gao S, Jia X, Li Z, Chen Y, Jiang K (2011) Antibiotic-inspired zinc oxide with morphology-dependent photocatalytic activity. *Can J Chem* 89:590–597. <https://doi.org/10.1139/V11-023/ASSET/IMAGES/LARGE/V11-023CON.JPEG>
- Gerbreder V, Krasovska M, Sledziskis E, Gerbreder A, Mihailova I, Tamanis E, Ogurcovs A (2020) Hydrothermal synthesis of ZnO nanostructures with controllable morphology change. *CrystEngComm* 22:1346–1358. <https://doi.org/10.1039/C9CE01556F>
- Han Z, Ren L, Cui Z, Chen C, Pan H, Chen J (2012) Ag/ZnO flower heterostructures as a visible-light driven photocatalyst via surface plasmon resonance. *Appl Catal B Environ* 126:298–305. <https://doi.org/10.1016/j.apcatb.2012.07.002>
- Hernández-Alonso MD, Fresno F, Suárez S, Coronado JM (2009) Development of alternative photocatalysts to TiO₂: challenges and opportunities. *Energy Environ Sci* 2:1231–1257. <https://doi.org/10.1039/B907933E>
- Hossienzadeh K, Maleki A, Daraei H, Safari M, Pawar R, Lee SM (2019) Sonocatalytic and photocatalytic efficiency of transition metal-doped ZnO nanoparticles in the removal of organic dyes from aquatic environments. *Korean J Chem Eng* 36:1360–1370. <https://doi.org/10.1007/s11814-019-0299-6>
- Hsu M-H, Chang C-J (2014) Ag-doped ZnO nanorods coated metal wire meshes as hierarchical photocatalysts with high visible-light driven photoactivity and photostability. *J Hazard Mater* 278:444–453. <https://doi.org/10.1016/j.jhazmat.2014.06.038>
- Huang H, Wang Y, Cai F, Jiao W, Zhang N, Liu C, Cao H, Lu J (2017) Photodegradation of rhodamine b over biomass-derived activated carbon supported CdS nanomaterials under visible irradiation. *Front Chem* 5:123. <https://doi.org/10.3389/fchem.2017.00123>
- Islam MR, Rahman M, Farhad SFU, Podder J (2019) Structural, optical and photocatalysis properties of sol – gel deposited Al- doped ZnO thin films. *Surf Interfaces* 16:120–126. <https://doi.org/10.1016/j.surfin.2019.05.007>
- Jadhav LD, Patil SP, Chavan AU, Jamale AP, Puri VR (2011) Solution combustion synthesis of Cu nanoparticles: a role of oxidant-to-fuel ratio. *Micro Nano Lett* 6:812. <https://doi.org/10.1049/mnl.2011.0372>
- Jiang Z-J, Liu C-Y, Sun L-W (2005) Catalytic properties of silver nanoparticles supported on silica spheres. *J Phys Chem B* 109:1730–1735. <https://doi.org/10.1021/jp046032g>
- Jiang J, Mu Z, Xing H, Wu Q, Yue X, Lin Y (2019) Insights into the synergetic effect for enhanced UV/visible-light activated photodegradation activity via Cu-ZnO photocatalyst. *Appl Surf Sci* 478:1037–1045. <https://doi.org/10.1016/j.apsusc.2019.02.019>
- Jongnavakit P, Amornpitoksuk P, Suwanboon S, Ratana T (2012) Surface and photocatalytic properties of ZnO thin film prepared by sol–gel method. *Thin Solid Films* 520:5561–5567. <https://doi.org/10.1016/J.TSF.2012.04.050>
- Kadam AN, Bhopate DP, Kondalkar VV, Majhi SM, Bathula CD, Tran AV, Lee SW (2018) Facile synthesis of Ag-ZnO core–shell nanostructures with enhanced photocatalytic activity. *J Ind Eng Chem* 61:78–86. <https://doi.org/10.1016/J.JIEC.2017.12.003>
- Kalita J, Das B, Dhar SS (2022) Synergistic effect of iron and copper in hydroxyapatite nanorods for Fenton-like oxidation of organic dye. *Coll Surf A Physicochem Eng Asp* 643:128750. <https://doi.org/10.1016/J.COLSURFA.2022.128750>
- Kant R (2012) Textile dyeing industry an environmental hazard. *Nat Sci* 04:22–26. <https://doi.org/10.4236/ns.2012.41004>
- Karunakaran C, Rajeswari V, Gomathisankar P (2011) Optical, electrical, photocatalytic, and bactericidal properties of microwave synthesized nanocrystalline Ag-ZnO and ZnO. *Solid State Sci* 13:923–928. <https://doi.org/10.1016/J.SOLIDSTATESCIEN CES.2011.02.016>
- Kasperchik VP, Yaskevich AL, Bilydukevich AV (2012) Wastewater treatment for removal of dyes by coagulation and membrane processes. *Pet Chem* 52:545–556. <https://doi.org/10.1134/S0965544112070079>
- Kayaci F, Vempati S, Donmez I, Biyikli N, Uyar T (2014) Role of zinc interstitials and oxygen vacancies of ZnO in photocatalysis: a bottom-up approach to control defect density. *Nanoscale* 6:10224–10234. <https://doi.org/10.1039/C4NR01887G>
- Kazeminezhad I, Sadollahkhani A (2016) Influence of pH on the photocatalytic activity of ZnO nanoparticles. *J Mater Sci Mater Electron* 27:4206–4215. <https://doi.org/10.1007/s10854-016-4284-0>
- Kumar A (2017) A review on the factors affecting the photocatalytic degradation of hazardous materials. *Mater Sci Eng Int J* 1:106–114. <https://doi.org/10.15406/mseij.2017.01.00018>
- Kumar R, Janbandhu SY, Sukhadeve GK, Gedam RS (2022) Visible light assisted surface plasmon resonance triggered Ag/ZnO nanocomposites: synthesis and performance towards degradation of indigo carmine dye. *Environ Sci Pollut Res*. <https://doi.org/10.1007/s11356-022-22745-y>
- Kuo SY, Chen WC, Lai FI, Cheng CP, Kuo HC, Wang SC, Hsieh WF (2006) Effects of doping concentration and annealing temperature on properties of highly-oriented Al-doped ZnO films. *J Cryst Growth* 287:78–84. <https://doi.org/10.1016/J.JCRYSGRO.2005.10.047>
- Lee HJ, Kim JH, Park SS, Hong SS, Lee GD (2015) Degradation kinetics for photocatalytic reaction of methyl orange over Al-doped ZnO nanoparticles. *J Ind Eng Chem* 25:199–206. <https://doi.org/10.1016/j.jiec.2014.10.035>
- Lim H-H, Chua P-N, Mun HPUI, Amini Horri B, Salamatinia B (2019) Synthesis and characterisation of cuo/hnt nano-particles through in-situ glycine nitrate process. *Int J Adv Sci Eng Technol* 6:24–28
- Liu L, Liu Z, Yang Y, Geng M, Zou Y, Shahzad MB, Dai Y, Qi Y (2018) Photocatalytic properties of Fe-doped ZnO electrospun nanofibers. *Ceram Int* 44:19998–20005. <https://doi.org/10.1016/J.CERAMINT.2018.07.268>
- Lu Y, Lin Y, Wang D, Wang L, Xie T, Jiang T (2011) A high performance cobalt-doped ZnO visible light photocatalyst and its photogenerated charge transfer properties. *Nano Res* 4:1144–1152. <https://doi.org/10.1007/s12274-011-0163-4>

- Luan J, Shen Y, Wang S, Guo N (2017) Synthesis, property characterization and photocatalytic activity of the polyaniline/BiYTiO₇ polymer composite. *Polymers (basel)*. <https://doi.org/10.3390/polym9030069>
- Luo JL, Wang SF, Liu W, Tian CX, Wu JW, Zu XT, Zhou WL, Yuan XD, Xiang X (2017) Influence of different aluminum salts on the photocatalytic properties of Al doped TiO₂ nanoparticles towards the degradation of AO7 dye. *Sci Rep* 7:1–16. <https://doi.org/10.1038/s41598-017-08216-2>
- Ma Q, Lv X, Wang Y, Chen J (2016) Optical and photocatalytic properties of Mn doped flower-like ZnO hierarchical structures. *Opt Mater (amst)* 60:86–93. <https://doi.org/10.1016/j.optmat.2016.07.014>
- Marin R, Oussta F, Katea SN, Prabhudev S, Botton GA, Westin G, Hemmer E (2019) Europium-doped ZnO nanosponges – controlling optical properties and photocatalytic activity. *J Mater Chem C* 7:3909–3919. <https://doi.org/10.1039/C9TC00215D>
- Mendoza-Mendoza E, Nuñez-Briones AG, García-Cerda LA, Peralta-Rodríguez RD, Montes-Luna AJ (2018) One-step synthesis of ZnO and Ag/ZnO heterostructures and their photocatalytic activity. *Ceram Int* 44:6176–6180. <https://doi.org/10.1016/J.CERAMINT.2018.01.001>
- Mika K, Socha RP, Nyga P, Wiercigroch E, Małek K, Jarosz M, Uchacz T, Sulka GD, Zaraska L (2019) Electrochemical synthesis and characterization of dark nanoporous zinc oxide films. *Electrochim Acta* 305:349–359. <https://doi.org/10.1016/J.ELECTACTA.2019.03.052>
- Mohammadzadeh S, Olya ME, Arabi AM, Shariati A, Khosravi Nikou MR (2015) Synthesis, characterization and application of ZnO-Ag as a nanophotocatalyst for organic compounds degradation, mechanism and economic study. *J Environ Sci* 35:194–207. <https://doi.org/10.1016/J.JES.2015.03.030>
- Moiz MA, Mumtaz A, Salman M, Mazhar H, Basit MA, Husain SW, Ramzan M (2021) Enhancement of dye degradation by zinc oxide via transition-metal doping: a review. *J Electron Mater* 50:5106–5121. <https://doi.org/10.1007/s11664-021-09093-2>
- Mouzaia F, Djouadi D, Chelouche A, Hammiche L, Touam T (2020) Particularities of pure and Al-doped ZnO nanostructures aerogels elaborated in supercritical isopropanol. *Arab J. Basic. Appl Sci* 27:423–430. <https://doi.org/10.1080/25765299.2020.1833484>
- Najjar M, Hosseini HA, Masoudi A, Sabouri Z, Mostafapour A, Khatami M, Darroudi M (2021) Green chemical approach for the synthesis of SnO₂ nanoparticles and its application in photocatalytic degradation of eriochrome black T dye. *Optik (stuttg)*. 242:167152. <https://doi.org/10.1016/j.ijleo.2021.167152>
- Naldoni A, Altomare M, Zoppellaro G, Liu N, Kment Š, Zbořil R, Schmuki P (2019) Photocatalysis with reduced TiO₂: from black TiO₂ to cocatalyst-free hydrogen production. *ACS Catal* 9:345–364. <https://doi.org/10.1021/acscatal.8b04068>
- Neppolian B, Choi HC, Sakthivel S, Arabindoo B, Murugesan V (2002) Solar light induced and TiO₂ assisted degradation of textile dye reactive blue 4. *Chemosphere* 46:1173–1181. [https://doi.org/10.1016/S0045-6535\(01\)00284-3](https://doi.org/10.1016/S0045-6535(01)00284-3)
- Nguyen LTT, Nguyen HTT, Nguyen LTH, Duong ATT, Nguyen HQ, Bui ND, Ngo VTM, Nguyen DTC, Van Tran T (2022) Toward enhanced visible-light photocatalytic dye degradation and reusability of La³⁺ substituted ZnFe₂O₄ nanostructures. *Environ Res* 214:114130. <https://doi.org/10.1016/J.ENVRES.2022.114130>
- Ntwaeaborwa OM, Mofokeng SJ, Kumar V, Kroon RE (2017) Structural, optical and photoluminescence properties of Eu³⁺ doped ZnO nanoparticles. *Spectrochim Acta Part A Mol Biomol Spectrosc* 182:42–49. <https://doi.org/10.1016/j.saa.2017.03.067>
- Park HW, Chung KB, Park JS, Ji S, Song K, Lim H, Jang MH (2015) Electronic structure of conducting Al-doped ZnO films as a function of Al doping concentration. *Ceram Int* 41:1641–1645. <https://doi.org/10.1016/J.CERAMINT.2014.09.102>
- Pascariu P, Homocianu M, Cojocaru C, Samoila P, Airinei A, Suche M (2019) Preparation of La doped ZnO ceramic nanostructures by electrospinning–calcination method: Effect of La³⁺ doping on optical and photocatalytic properties. *Appl Surf Sci* 476:16–27. <https://doi.org/10.1016/J.APSUSC.2019.01.077>
- Paul DR, Sharma R, Nehra SP, Sharma A (2019) Effect of calcination temperature, pH and catalyst loading on photodegradation efficiency of urea derived graphitic carbon nitride towards methylene blue dye solution. *RSC Adv* 9:15381–15391. <https://doi.org/10.1039/C9RA02201E>
- Prabhuraj T, Prabhu S, Dhandapani E, Duraisamy N, Ramesh R, Kumar KAR, Maadeswaran P (2021) Bifunctional ZnO sphere/r-GO composites for supercapacitor and photocatalytic activity of organic dye degradation. *Diam Relat Mater* 120:108592. <https://doi.org/10.1016/j.diamond.2021.108592>
- Pramanik S, Mukherjee S, Dey S, Mukherjee S, Das S, Ghosh T, Ghosh P, Nath R, Kuiri PK (2022) Cooperative effects of zinc interstitials and oxygen vacancies on violet-blue photoluminescence of ZnO nanoparticles: UV radiation induced enhanced latent fingerprint detection. *J Lumin* 251:119156. <https://doi.org/10.1016/j.jlumin.2022.119156>
- Prasad R, Bhame SD, Walke P (2018) Structural and Optical Studies on Nanosized Thermoelectric Oxide-Zn_{1-x}Al_xO. *Int J Nanosci* 18:1850038. <https://doi.org/10.1142/S0219581X18500382>
- Prasad R, Walke PS, Bhame SD (2019) Facile one-pot synthesis of homologous (ZnO)_k.In₂O₃ based thermoelectric ceramics (k = 3, 5 & 7) by glycine nitrate combustion method and their potential application in photocatalysis. *Mater Res Express*. 6:085054. <https://doi.org/10.1088/2053-1591/ab1dec>
- Rafiq A, Ikram M, Ali S, Niaz F, Khan M, Khan Q, Maqbool M (2021) Photocatalytic degradation of dyes using semiconductor photocatalysts to clean industrial water pollution. *J Ind Eng Chem* 97:111–128. <https://doi.org/10.1016/J.JIEC.2021.02.017>
- Rajendran S, Mansoob Khan M, Gracia F, Qin J, Gupta VK, Arumainathan S (2016) Ce³⁺-ion-induced visible-light photocatalytic degradation and electrochemical activity of ZnO/CeO₂ nanocomposite. *Sci Rep*. 6:31641. <https://doi.org/10.1038/srep31641>
- Rajput RB, Jamble SN, Kale RB (2022) A review on TiO₂/SnO₂ heterostructures as a photocatalyst for the degradation of dyes and organic pollutants. *J Environ Manage* 307:114533. <https://doi.org/10.1016/J.JENVMAN.2022.114533>
- Retamoso C, Escalona N, González M, Barrientos L, Allende-González P, Stancovich S, Serpell R, Fierro JLG, Lopez M (2019) Effect of particle size on the photocatalytic activity of modified rutile sand (TiO₂) for the discoloration of methylene blue in water. *J Photochem Photobiol A Chem* 378:136–141. <https://doi.org/10.1016/J.JPHOTOCHEM.2019.04.021>
- Safeen A, Safeen K, Shafique M, Iqbal Y, Ahmed N, Rauf Khan MA, Asghar G, Althubeiti K, Al Otaibi S, Ali G, Shah WH, Khan R (2022) The effect of Mn and Co dual-doping on the structural, optical, dielectric and magnetic properties of ZnO nanostructures. *RSC Adv* 12:11923–11932. <https://doi.org/10.1039/d2ra01798a>
- Saidani T, Zaabat M, Aida MS, Barille R, Rasheed M, Almohamed Y (2017) Influence of precursor source on sol–gel deposited ZnO thin films properties. *J Mater Sci Mater Electron* 28:9252–9257. <https://doi.org/10.1007/s10854-017-6660-9>
- Salama A, Mohamed A, Aboamara NM, Khattab TAOA (2018) Photocatalytic degradation of organic dyes using composite nanofibers under UV irradiation. *Appl Nanosci* 8:155–161. <https://doi.org/10.1007/s13204-018-0660-9>
- Selvaraj S, Patrick SD, Vangari GA, Mohan MK, Ponnu S, Muthu C (2022) Facile synthesis of Sm doped ZnO nanoflowers by Co-precipitation method for enhanced photocatalytic degradation of

- MB dye under sunlight irradiation. *Ceram Int* 48:29049–29058. <https://doi.org/10.1016/j.ceramint.2022.04.299>
- Shah A, Ahmad M, Rahmanuddin S, Khan U, Aziz Z, Ali A, Khan AM (2019) The role of Al doping on ZnO nanowire evolution and optical band gap tuning. *Appl Phys A Mater Sci Process* 125:1–8. <https://doi.org/10.1007/s00339-019-3005-y>
- Shah AA, Bhatti MA, Tahira A, Chandio AD, Channa IA, Sahito AG, Chalangar E, Willander M, Nur O, Ibupoto ZH (2020) Facile synthesis of copper doped ZnO nanorods for the efficient photo degradation of methylene blue and methyl orange. *Ceram Int* 46:9997–10005. <https://doi.org/10.1016/J.CERAMINT.2019.12.024>
- Sharma R, Bansal S, Singhal S (2015) Tailoring the photo-Fenton activity of spinel ferrites (MFe₂O₄) by incorporating different cations (M = Cu, Zn, Ni and Co) in the structure. *RSC Adv* 5:6006–6018. <https://doi.org/10.1039/C4RA13692F>
- Sohrabnezhad S, Seifi A (2016) The green synthesis of Ag/ZnO in montmorillonite with enhanced photocatalytic activity. *Appl Surf Sci* 386:33–40. <https://doi.org/10.1016/J.APSUSC.2016.05.102>
- Speaks DT (2020) Effect of concentration, aging, and annealing on sol gel ZnO and Al-doped ZnO thin films. *Int J Mech Mater Eng.* <https://doi.org/10.1186/s40712-019-0113-6>
- Tabti S, Benchettara A, Smaili F, Benchettara A, Berrabah SE (2022) Electrodeposition of lead dioxide on Fe electrode: application to the degradation of Indigo Carmine dye. *J Appl Electrochem* 52:1207–1217. <https://doi.org/10.1007/s10800-022-01709-7>
- Thamaraiselvan C, Noel M (2015) Membrane processes for dye wastewater treatment: recent progress in fouling control. *Crit Rev Environ Sci Technol* 45:1007–1040. <https://doi.org/10.1080/10643389.2014.900242>
- Tripathy N, Kim D-H (2018) Metal oxide modified ZnO nanomaterials for biosensor applications. *Nano Converg* 5:27. <https://doi.org/10.1186/s40580-018-0159-9>
- Umar K, Mfarrej MFB, Rahman QI, Zuhaib M, Khan A, Zia Q, Banawas S, Nadeem H, Khan MF, Ahmad F (2022) ZnO Nanoswirlings for azo dye AR183 photocatalytic degradation and antimicrobial activity. *Sci Rep* 12:14023. <https://doi.org/10.1038/s41598-022-17924-3>
- Venkatachalam S, Iida Y, Kanno Y (2008) Preparation and characterization of Al doped ZnO thin films by PLD. *Superlattices Microstruct* 44:127–135. <https://doi.org/10.1016/j.spmi.2008.03.006>
- Vijayalakshmi K, Sivaraj D (2015) Enhanced antibacterial activity of Cr doped ZnO nanorods synthesized using microwave processing. *RSC Adv.* 5:68461. <https://doi.org/10.1039/c5ra13375k>
- Wahba MA, Yakout SM, Mohamed WAA, Galal HR (2020) Remarkable photocatalytic activity of Zr doped ZnO and ZrO₂/ZnO nanocomposites: Structural, morphological and photoluminescence properties. *Mater Chem Phys* 256:123754. <https://doi.org/10.1016/j.matchemphys.2020.123754>
- Wang SS, Xu AW (2012) Template-free facile solution synthesis and optical properties of ZnO mesocrystals. *CrystEngComm* 15:376–381. <https://doi.org/10.1039/C2CE26638E>
- Wang J, Hou S, Zhang L, Chen J, Xiang L (2014) Ultra-rapid formation of ZnO hierarchical structures from dilution-induced supersaturated solutions. *CrystEngComm* 16:7115–7123. <https://doi.org/10.1039/C4CE00765D>
- Yadav RS, Mishra P, Pandey AC (2010) Tuning the band gap of ZnO nanoparticles by ultrasonic irradiation. *Inorg Mater* 46(2):163–167. <https://doi.org/10.1134/S0020168510020135>
- Yang Y, Chun Y, Shang G, Huang M (2004) pH-dependence of pesticide adsorption by wheat-residue-derived black carbon. *Langmuir* 20:6736–6741. <https://doi.org/10.1021/la049363t>
- Yuan Z, Jiaqiang X, Qun X, Hui L, Qingyi P, Pengcheng X (2009) Brush-like hierarchical zno nanostructures: synthesis, photoluminescence and gas sensor properties. *J Phys Chem C* 113:3430–3435. https://doi.org/10.1021/JP8092258/ASSET/IMAGES/LARGE/JP-2008-092258_0012.JPEG
- Yudasari N, Tresna WP, Sugiarto IT, Irmawati Y, Suhandi A, Isnaeni (2022) Photocatalytic degradation of blue dyes using simple and biocompatible synthesized ZnO Nanorods/Zn photocatalysts under tube luminescent lamp. *Int. Conf. Adv. Mater. Technol.* 2708:050002. <https://doi.org/10.1063/5.0106465>
- Zhang D-F, Sun L-D, Zhang J, Yan Z-G, Yan C-H (2008) Hierarchical construction of ZnO architectures promoted by heterogeneous nucleation. *Cryst Growth Des* 8:3609–3615. <https://doi.org/10.1021/cg800143x>
- Zhao J, Wang L, Yan X, Yang Y, Lei Y, Zhou J, Huang Y, Gu Y, Zhang Y (2011) Structure and photocatalytic activity of Ni-doped ZnO nanorods. *Mater Res Bull* 46:1207–1210. <https://doi.org/10.1016/j.materresbull.2011.04.008>
- Zhu H, Jiang R, Fu Y, Guan Y, Yao J, Xiao L, Zeng G (2012) Effective photocatalytic decolorization of methyl orange utilizing TiO₂/ZnO/chitosan nanocomposite films under simulated solar irradiation. *Desalination* 286:41–48. <https://doi.org/10.1016/J.DESAL.2011.10.036>
- Zouhier M, Tanji K, Navio JA, Hidalgo MC, Jaramillo-Páez C, Kherbeche A (2020) Preparation of ZnFe₂O₄/ZnO composite: Effect of operational parameters for photocatalytic degradation of dyes under UV and visible illumination. *J Photochem Photobiol A Chem* 390:112305. <https://doi.org/10.1016/J.JPHOTOCHEM.2019.112305>

Publisher's Note Springer Nature remains neutral with regard to jurisdictional claims in published maps and institutional affiliations.